Mechanism for normal faulting in the subducting plate at the Mariana Trench

Zhiyuan Zhou[1,2], Jian Lin[1,2,3], Mark D. Behn[2], and Jean-Arthur Olive[4,5]

[1]State Key Laboratory of Marine Geology, School of Ocean and Earth Sciences, Tongji University, Shanghai, China, [2]Department of Geology and Geophysics, Woods Hole Oceanographic Institution, Woods Hole, Massachusetts, USA, [3]Key Laboratory of Marginal Sea Geology, Chinese Academy of Sciences, South China Sea Institute of Oceanology, Guangzhou, China, [4]MIT/WHOI Joint Program in Oceanography, Massachusetts Institute of Technology, Woods Hole, Massachusetts, USA, [5]Now at Lamont-Doherty Earth Observatory, Columbia University, Palisades, New York, USA

Abstract We investigate the mechanisms of normal fault initiation and evolution in the subducting Pacific Plate near the Mariana Trench, through bathymetry analysis and geodynamic modeling. We model the subducting plate as an elastoplastic slab subjected to tectonic forcing at the trench, including vertical load, bending moment, and horizontal tensional force. In our simulations, normal faults initiate within the outer rise region and reach maximum throw toward the trench. This result holds over a wide range of tectonic forcing and is consistent with observations of the Challenger Deep region, where multibeam bathymetry data indicate faults initiate near the outer rise at 70–110 km from the trench and reach maximum throw at 10–35 km from the trench. However, models require a horizontal tensional force with magnitude comparable to axial vertical load to jointly explain the observed seafloor bathymetry, location of maximum normal fault throw, and prevalence of normal faults dipping toward the trench.

1. Introduction

During subduction, the downgoing slab flexes, generating significant flexural stresses in the plate. The bending of the plate influences processes such as the formation of normal faults, intraslab seismicity, and hydration of the slab [e.g., *Savage*, 1969; *Frohlich*, 1989; *Kirby et al.*, 1996; *Ranero et al.*, 2003, 2005; *Ivandic et al.*, 2008; *Faccenda et al.*, 2008, 2009; *Emry et al.*, 2014]. Moreover, normal faulting earthquakes at the outer rise region of a subduction zone can pose significant seismic and tsunami hazard [e.g., *Kobayashi et al.*, 1998; *Choy and Kirby*, 2004; *Lay et al.*, 2009, 2010].

Previous studies have recognized the important role of flexure in generating normal faults in the downgoing slab [e.g., *Ludwig et al.*, 1966; *Jones et al.*, 1978; *Masson*, 1991; *Kobayashi et al.*, 1998; *Ranero et al.*, 2003; *Supak et al.*, 2006; *Ivandic et al.*, 2008; *Naliboff et al.*, 2013]. Furthermore, the formation of normal faults feeds back to influence the flexural behavior of the plate. *Billen and Gurnis* [2005], *Contreras-Reyes and Osses* [2010], and *Zhang et al.* [2014] proposed that the effective elastic thickness of the lithosphere T_e is significantly reduced trenchward of the outer rise region as reflected in the observed steep flexural shape approaching the trench axis. *Zhang et al.* [2014] further calculated that T_e of the subducting Pacific Plate is reduced by 40–60% near the Mariana Trench due to normal faulting.

Several analog and numerical studies have investigated fault formation in response to bending. *Supak et al.* [2006] conducted analog experiments and found that normal faults are first initiated along an axis of maximum bending stress and then link along strike. *Faccenda et al.* [2008, 2009] simulated normal faulting in a 2-D viscoelastoplastic plate and investigated fault-driven slab hydration. *Naliboff et al.* [2013] conducted 2-D viscoplastic numerical experiments and found that normal faulting characteristics could be influenced by the age and velocity of the subducting plate, coupling at plate interface, and slab pull, while spatial variations in friction coefficient are less important. However, the feedback mechanisms among plate flexure, fault formation, and the evolving strength of the plate due to faulting are still poorly understood.

In this study, we conduct numerical experiments to investigate normal fault initiation and evolution in a 2-D elastoplastic plate subjected to trench axis vertical load, bending moment, and horizontal tensional force. The models are constrained using the observed bathymetry as well as the location, throw, and dipping

direction of normal faults of the Mariana Trench. We find that the long-wavelength bathymetry at the Mariana Trench can be explained by a wide range of plate bending models involving only vertical load and bending moment at the trench axis. However, to explain the observed normal faulting characteristics, the bending plate must also be subjected to a significant horizontal tensional force.

2. Observed Normal Faults Near the Mariana Trench

The Mariana Trench is located in the western Pacific Ocean, where the Pacific Plate subducts beneath the Mariana and Philippine Plates at convergence rates of 4–8 cm/yr (Figure 1a and Figure S1 in the supporting information). We identify seafloor normal faults in three regions along the Mariana Trench (Figure 1a), where high-resolution multibeam bathymetry data are available. The majority of seafloor normal fault scarps are subparallel to the local strike of the Mariana Trench axis (Figure S1) and oblique to crustal age isochrons (Figure 1a). This indicates that normal faults are predominantly controlled by subduction-related stresses rather than by inherited abyssal hill fabrics in the subducting plate.

We analyze trench-perpendicular profiles and calculate fault throw and density in the northern, central, and southern Mariana regions (Figure S1). Surface scarps of normal faults are identified using both topographic slope maps and individual topographic profiles. Normal faults first become visible at the outer rise region (Figure S1), and fault throw and density then increase approaching the trench axis, reaching peak values trenchward of the outer rise (Figures 1b–1g).

There are, however, significant variations in normal faulting characteristics among the three regions (Figures 1b–1g). Fault throws in the southern region are larger than in the northern and central regions (Figures 1b–1d). The initiation distance of identifiable normal faults is about 85, 65, and 110 km from the trench for the northern, central, and southern regions, respectively (Figures 1b–1d). Maximum fault throw is reached close to the trench, at an average distance from the trench of about 5, 5, and 20 km for the northern, central, and southern regions, respectively (Figures 1b–1d). In the southern region, fault density increases rapidly from 120 to 75 km from the trench axis and then remains relatively constant toward the trench (Figure 1g).

3. Numerical Modeling

We model elastoplastic deformation of a 2-D subducting plate using the explicit Lagrangian method FLAC (Fast Lagrangian Analysis of Continua) [*Cundall*, 1989; *Poliakov et al.*, 1993]. FLAC is ideal for simulating nonlinear rheological behavior of lithospheric deformation and has been used to investigate faulting in extensional settings [e.g., *Buck and Poliakov*, 1998; *Poliakov and Buck*, 1998; *Lavier et al.*, 1999, 2000; *Buck et al.*, 2005; *Behn and Ito*, 2008; *Tucholke et al.*, 2008; *Olive et al.*, 2010], as well as subduction zones [e.g., *Babeyko et al.*, 2002]. FLAC makes simultaneous predictions of topography and fault characteristics, allowing us to compare model results directly with observations at the Mariana Trench.

The computational domain spans 1200 km horizontally and 68 km vertically (Figure 2a). The subducting elastoplastic (brittle) plate and the underlying asthenospheric low-viscosity layer are defined by the imposed temperature structure, which increases linearly from 0°C at the surface to 450°C at the bottom of the plate and then increases abruptly to 1300°C for the whole asthenospheric layer. This results in a sharp brittle-ductile transition, minimizing the effect of viscous coupling at the base of the plate. We model a subducting plate of initial elastic thickness $T_e = 48$ km overlying a 20 km thick asthenospheric layer (Figure 2a). This value of T_e is consistent with the thickness of the incoming plate far from the trench based on flexural models of *Zhang et al.* [2014].

Brittle failure occurs according to a Mohr-Coulomb criterion assuming a friction coefficient of $\mu = 0.58$ and a cohesion of $C_0 = 44$ MPa. As plastic strain accumulates in a localized yield zone, cohesion drops linearly with the amount of plastic strain. When a critical plastic strain ε_c is reached, cohesion is assumed to retain a minimum value of $C_1 = 4$ MPa. To facilitate rapid strain localization, we use a smaller critical plastic strain ε_c than that used in previous models of extensional faulting [e.g., *Buck et al.*, 2005]; other model parameters (Table 1) follow *Lavier et al.* [2000].

The horizontal grid spacing is 0.5 km over the leftmost 250 km of the model domain, which encompasses the trench and the outer rise, and 9.8 km for the remaining 950 km of the domain. The vertical grid spacing is
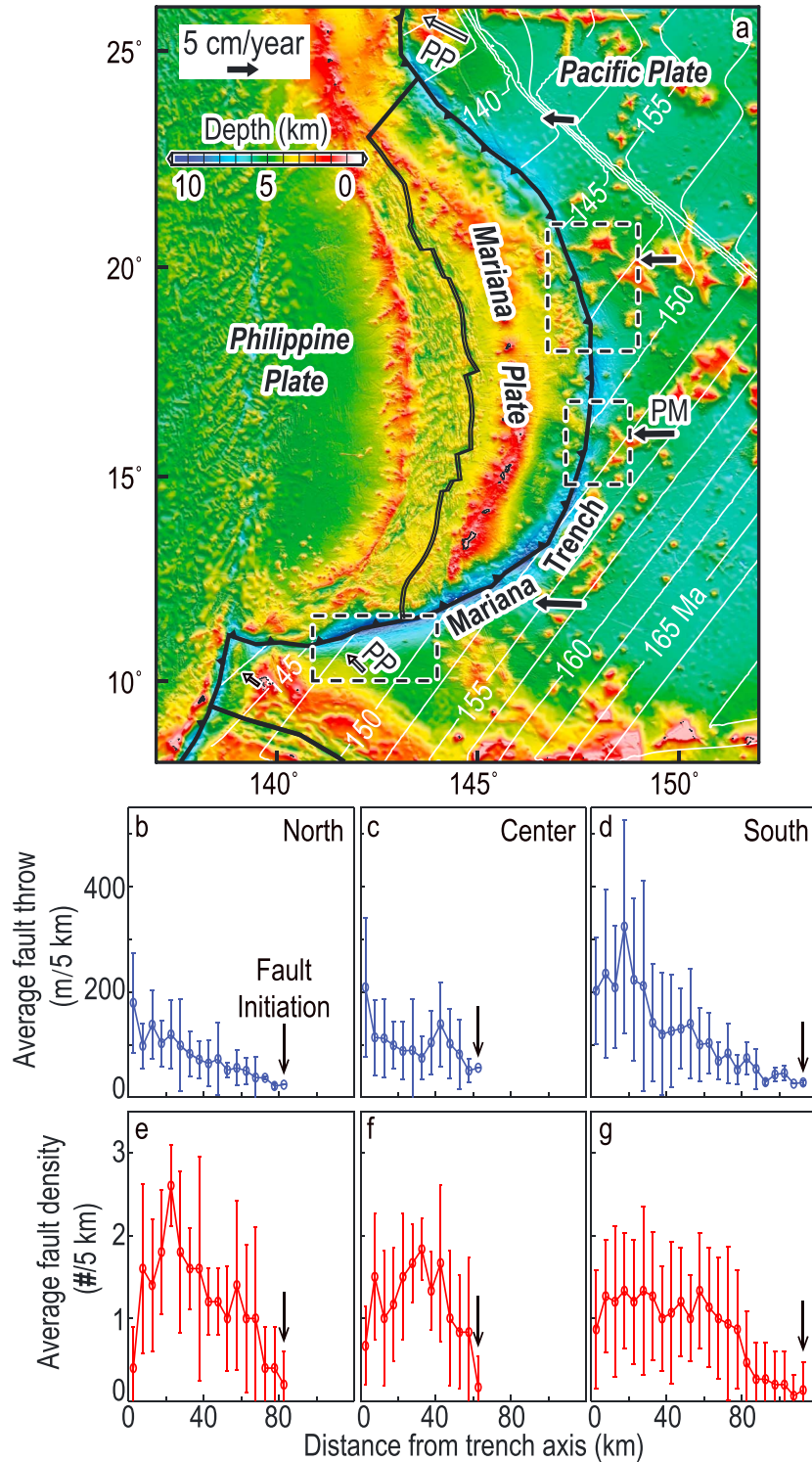
Figure 1. (a) Location of the Mariana Trench. Dashed boxes indicate areas where we analyzed high-resolution multibeam bathymetry data with average grid spacing of 65 m. White lines show crustal age contours of the Pacific Plate. Solid black and hollow black arrows indicate the velocity of the Pacific Plate relative to the Mariana Plate (PM) and the Philippine Plate (PP), respectively. (b–g) Calculated average normal fault throw and fault density per 5 km profile length as a function of distance from the trench axis for the northern, central, and southern Mariana Trench.
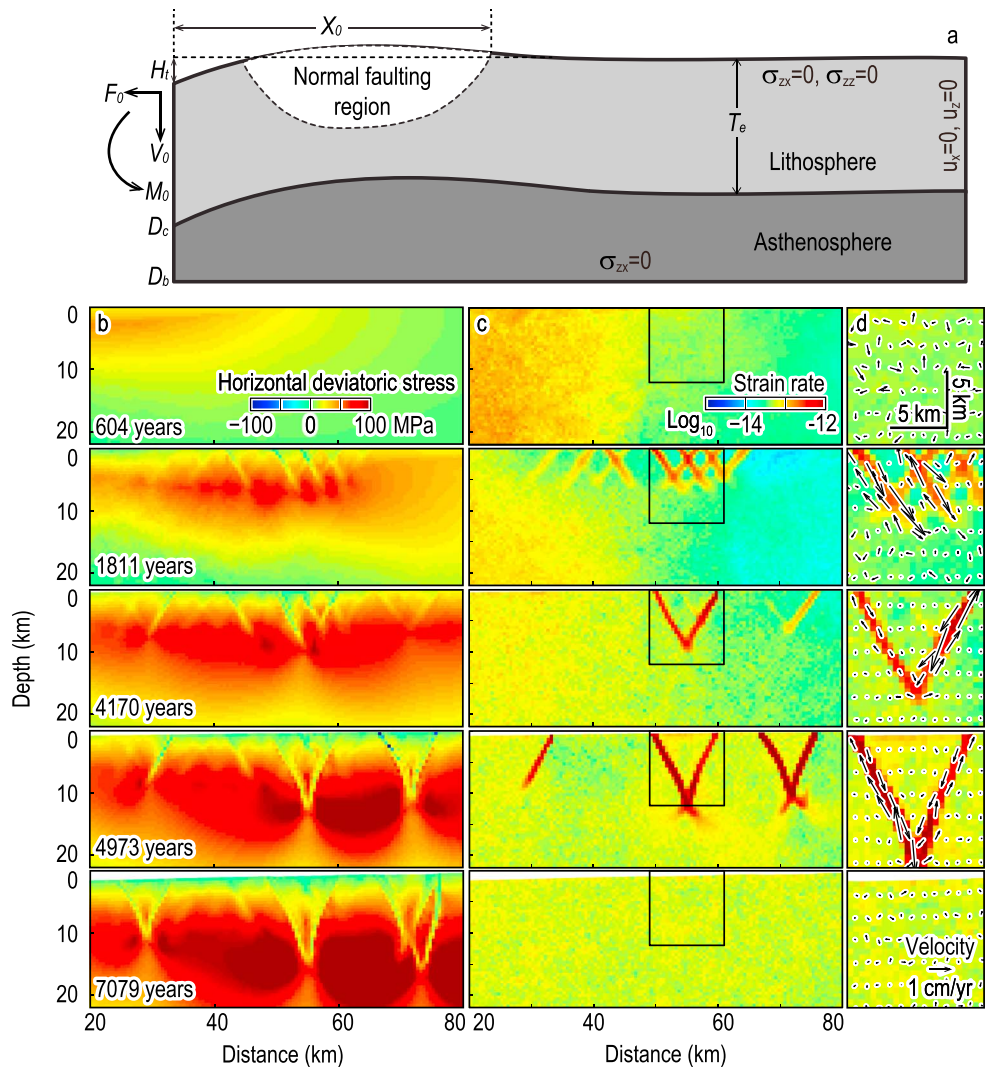
Figure 2. (a) Model setup with boundary conditions. The subducting plate is elastoplastic, while the underlying asthenospheric layer is viscous. Trench relief H_t and fault initiation distance X_0 are analyzed in detail. (b–d) Calculated evolution of normal fault growth as a function of time after loading. Figure 2b shows the calculated deviatoric stress field of the subducting plate. Figure 2c shows the corresponding strain rate. Figure 2d shows enlarged areas of boxes in Figure 2c. Black arrows show the velocity of each grid point relative to its adjacent points.

0.5 km within the lithospheric plate and 2 km in the asthenospheric layer. The surface of the plate is assumed to be stress free, while the basal boundary is lithostatic. The right-hand (oceanward) boundary of the plate is fixed with zero displacement. We applied depth-dependent shear and normal stresses at the left-hand (trenchward) boundary to simulate three types of tectonic forcing at the trench axis: vertical load V_0, bending moment M_0, and horizontal tensional force F_0.

4. Model Results

4.1. Normal Fault Initiation and Growth

The subducting plate flexes under trench axis loading, resulting in extensional (defined as positive) horizontal deviatoric stresses σ_{xx} in the upper part of the plate (Figure 2b). When the differential stress reaches the critical cohesion for failure, fault-like shear zones start to form and the plate begins to deform elastoplastically until deformation reaches a steady state (Figures 2b–2d). After an equilibrium state is reached, the trench no longer deepens and the plate deformation field no longer changes with time.

Table 1. Model Parameters

Parameters	Description	Value
T_e	Initial thickness of the lithosphere (km)	42–60
E	Young's modulus (Pa)	7.5×10^{10}
g	Gravitational acceleration (m/s^2)	9.81
v	Poisson's ratio	0.25
ρ	Density of lithosphere (kg/m^3)	3300
τ	Shear stress (MPa)	
σ_n	Normal stress (MPa)	
μ	Friction coefficient	0.58
T	Temperature (°C)	0–1300
V_0	Vertical load (N/m)	0–6.7×10^{12}
F_0	Horizontal tensional force (N/m)	0–9.6×10^{12}
M_0	Bending moment (N)	0–1.2×10^{17}
C_0	Initial cohesion of brittle material (MPa)	44
C_1	Remaining cohesion (MPa)	4
ε_c	Critical plastic strain	0.03

The calculated strain rates (Figure 2c) and relative velocities (Figure 2d) reveal a series of shear zones in the upper plate, which resemble normal faults. Bending induces extensional stresses in the upper plate (Figures 2b and 2c). Faults penetrate progressively to greater depth through time until an equilibrium state is achieved. We infer that in a subducting plate, normal faults will first form at the outer rise and then continue to grow as the plate moves toward the trench axis.

4.2. Sensitivity to Tectonic Forcing

We calculated the sensitivity of the model topography and normal faulting pattern to the three types of tectonic forcing (V_0, M_0, and F_0). We ran 567 models with various forcing combinations that fully span the range of observations, namely $V_0 = 0$–6.7×10^{12} N/m, $M_0 = 0$–1.2×10^{17} N, and $F_0 = 0$–9.6×10^{12} N/m. From the calculated topography, we determined the trench relief H_t and the fault initiation distance from the trench axis X_0 (Figure 2a). The calculated H_t increases with increasing V_0, M_0, and F_0 (Figures 3a–3c). In some cases, normal faults cut through the entire plate, breaking the plate into two parts (top right white regions in Figure 3). H_t observed at the southern Mariana Trench is 4.3–5.3 km, and X_0 is 70–110 km, respectively. We find that a combination of V_0, M_0, and F_0 can explain the observed H_t of the southern Mariana Trench (red dashed lines, Figures 3a–3c). Similarly, the calculated X_0 generally increases with V_0, M_0, and F_0, but the results are more scattered because X_0 is more difficult to define for a plate containing discrete faults. Again, a range of values of V_0, M_0, and F_0 can explain the observed X_0 of the southern Mariana Trench (red dashed lines, Figures 3d–3f).

5. Application to the Southern Mariana Trench

5.1. Constraints From Nonisostatic Topography

We next compare our model predictions to the observed topography and normal faulting characteristics of the southern Mariana Trench. The topography of the subducting plate reflects not only the flexural response to plate bending but also isostatic response to lateral variations in sediment thickness, crustal thickness, and mantle temperature [*Zhang et al.*, 2014]. Thus, we compare our model results with nonisostatic topography, which was calculated by removing from the observed topography the effects of (1) sediment loading, (2) isostatically compensated topography, and (3) thermal subsidence [*Zhang et al.*, 2014].

We focus only on the southern Mariana Trench for two reasons: (1) this region has fewer seamounts than the central and northern regions; and (2) the area of available high-resolution bathymetry data is significantly greater than in the central and northern regions (Figure S1), thus facilitating comparison with models. We averaged 15 profiles of nonisostatic topography at the southern Mariana Trench into a single reference profile to minimize the effect of short-wavelength variations along the individual profiles. Both the observed and modeled topographies display high-frequency variability associated with faulting; they are smoothed using a second-order polynomial model (Figure 4a). We calculate the root-mean-square (RMS) difference between the nonisostatic and modeled topography as a function of V_0, M_0, and F_0 (Figure S2). The red dashed contours in Figure S2 outline the combination of model parameters yielding an RMS of less than 150 m. Thus, the calculated nonisostatic topography can be explained by a range of tectonic forcing: V_0 in range of 5.7–6.2 $\times 10^{12}$ N/m, M_0 of 7.7–11.5 $\times 10^{16}$ N, and F_0 of 2.4–4.8 $\times 10^{12}$ N/m.

5.2. Constraints From Normal Faulting Characteristics

The previous section illustrated that a range of tectonic forcing parameters can equally well fit the observed nonisostatic topography. Here we use two additional lines of evidence to further constrain the tectonic
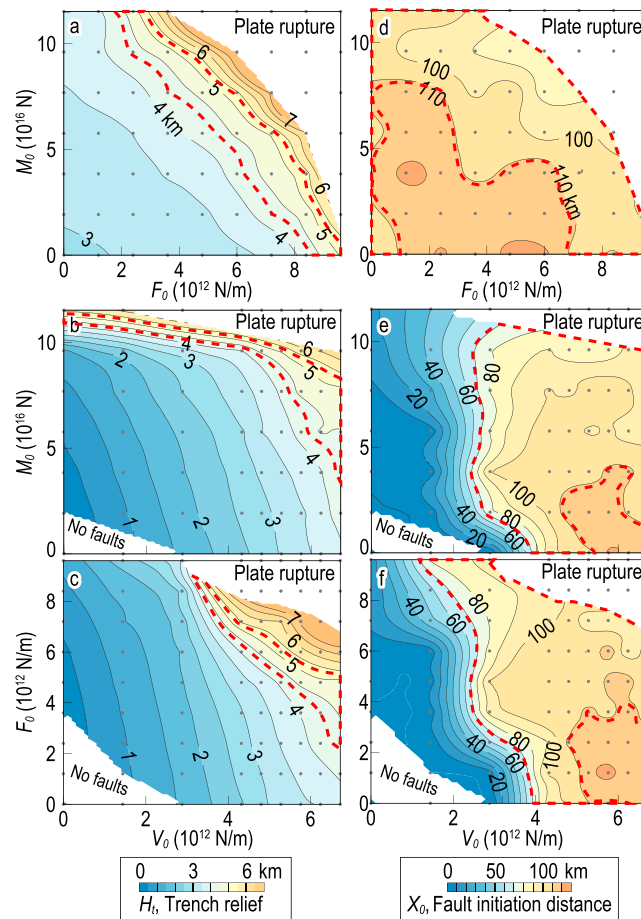
Figure 3. Calculated trench relief H_t and fault initiation distance from the trench axis X_0 as a function of the applied tectonic forcing. In each panel, the top right white regions mark cases when normal faults cut through the entire plate, while the bottom left white regions indicate cases when applied forces were too small to generate normal faults. Red dashed lines indicate observations at the southern Mariana Trench. Grey points indicate individual model calculations. (a and d) $V_0 = 5.8 \times 10^{12}$ N/m, (b and e) $F_0 = 4.8 \times 10^{12}$ N/m, (c and f) $M_0 = 7.7 \times 10^{16}$ N.

forcing: (1) the magnitude and spatial variations of normal fault throw as a function of distance from the trench and (2) the prevalence of normal faults dipping toward the trench [*Ranero et al.*, 2003; *Oakley et al.*, 2008]. In general, models with F_0 are a better fit to the observed fault throw than models without F_0 (Figure 4b), which is consistent with models of *McNutt and Menard* [1982] with significant horizontal forces in the subducting plate. In particular, the topographic best fitting model without F_0 predicts maximum fault throw to occur at about 50 km from the trench axis, which is inconsistent with the observation of maximum fault throw at an average distance of ~20 km from the southern Mariana Trench (Figure 4b). Furthermore, models with F_0 predict normal faults dipping predominantly toward the trench, which is consistent with observations of the southern Mariana Trench, while models without F_0 predict both trenchward and oceanward dipping faults (Figures 4c–4f).

In conclusion, while the calculated non-isostatic topography at the southern Mariana Trench can be adequately explained by models involving only trench axis vertical load and bending moment, the observed normal faulting characteristics can only be explained by models that also involve a significant horizontal tensional force (Figure 4).

The best fitting model for the southern Mariana Trench requires a vertical load $V_0 \sim 5.8 \times 10^{12}$ N/m and a horizontal tensional force $F_0 \sim 3.6 \times 10^{12}$ N/m, which is about 62% of the trench axis vertical load.

6. Discussion

The best fitting V_0 from our analysis is about 80% greater than that of the *Zhang et al.* [2014] model of the southern Mariana Trench. This is understandable because our models require a larger vertical load to break the plate, while *Zhang et al.* [2014] modeled a plate that already has reduced T_e due to pervasive faulting. The vertical load V_0 and horizontal tensional force F_0 could be considered two components of the downdip slab pull. Under this assumption, our best estimates of the vertical load and horizontal tensional force predict a slab pull force dipping ~58° with a magnitude of ~6.8×10^{12} N/m. This value is in good agreement with the order of magnitude (10^{13} N/m) predicted from scaling analysis [*Forsyth and Uyeda*, 1975]. We hypothesize that the inferred horizontal tensional forces for the southern Mariana Trench might result from the negative buoyancy of the deeper part of the subducted slab that is transmitted to the shallower part of the plate. Furthermore, we note that the efficient force transmission may be facilitated by a relatively low degree of mechanical coupling along the plate interface, which is potentially manifest as a paucity of large megathrust earthquakes at the Mariana Trench [*Okal et al.*, 2013].

Figure 4. Comparison of the topographic best fitting models (TBFM) to nonisostatic topography of the southern Mariana Trench. For TBFM with F_0, $V_0 = 5.8 \times 10^{12}$ N/m, $M_0 = 9.6 \times 10^{16}$ N, and $F_0 = 3.6 \times 10^{12}$ N/m; for TBFM without F_0, $V_0 = 6.7 \times 10^{12}$ N/m, and $M_0 = 1.2 \times 10^{17}$ N. (a) Comparison of best fitting model topography, with and without F_0, and the calculated average nonisostatic topography of the southern Mariana Trench. (b) Comparison of distribution of fault throw as a function of distance from the trench axis. (c) Calculated topography and (d) horizontal deviatoric stress σ_{xx} for TBFM without F_0. (e) Calculated topography and (f) horizontal deviatoric stress σ_{xx} for TBFM with F_0. In Figures 4c and 4e, magenta arrows indicate outward dipping normal faults, while green arrows indicate inward dipping normal faults.

The model results above correspond to an initial plate thickness of 48 km. However, *Zhang et al.* [2014] found variations in plate thickness approaching the trench. Thus, to further investigate the influence of T_e on plate flexure, we run a set of models with T_e values ranging from 42 km to 60 km, focusing on the effect on trench relief. Model results suggest that the calculated trench relief is more sensitive to V_0 for a thin plate (e.g., $T_e = 42$ km, Figure 5a) than for a thicker plate ($T_e \geq 48$ km). The calculated trench relief also increases with F_0 and M_0 more rapidly for a thinner plate (Figures 5b and 5c).

For an elastic plate with uniform thickness, the calculated trench relief H_t is given by *Turcotte and Schubert* [2002]: $H_t = (V_0\alpha + M_0)\frac{\alpha^2}{2D}$, where α is the flexural wavelength of the plate, D is its flexural rigidity; α and D depend only on T_e, and α^2/D and α^3/D scale as $Te^{-3/2}$ and $Te^{-3/4}$, respectively. Thus, the trench relief should increase linearly with V_0 and M_0 for a uniform thickness elastic plate. We therefore conclude that
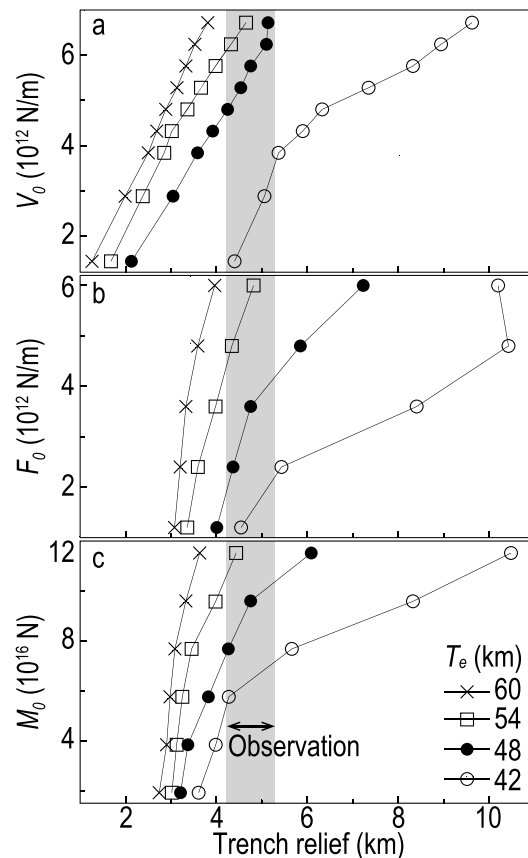
Figure 5. The calculated trench relief as a function of tectonic forcing for various assumed elastic plate thickness T_e. Grey column indicates the observed trench relief of the southern Mariana Trench. (a) $F_0 = 3.6 \times 10^{12}$ N/m, $M_0 = 9.6 \times 10^{16}$ N; (b) $V_0 = 5.7 \times 10^{12}$ N/m, $M_0 = 9.6 \times 10^{16}$ N; (c) $V_0 = 5.8 \times 10^{12}$ N/m, $F_0 = 3.6 \times 10^{12}$ N/m.

deviation from the linear trend in Figure 5 implies inelastic behavior, i.e., indicating a reduction in T_e due to formation of normal faults, which is more pronounced in thinner plates.

In best fitting models with significant horizontal tensional force (Figure 4f), most of the normal faults are calculated to extend to depths greater than 20 km, which are much deeper than the nominal crustal thickness of 6 km. Consequently, if normal faults can act as efficient fluid pathways, then a significant amount of water may reach the lithospheric upper mantle at the southern Mariana Trench. This could allow significant slab hydration through serpentinization reactions, with important consequences on the volatile budget and magmatic processes at this subduction zone [e.g., *Van Keken et al.*, 2011].

7. Conclusions

The majority of bending-related normal faults are found to be subparallel to the local strike of the Mariana Trench axis, indicating that the orientation of normal faults is predominantly controlled by subduction-related stresses rather than by inherited abyssal hill fabrics in the subducting plate. Results of analyses reveal that the majority of normal faults initiate near the outer rise, about 70–110 km away from the axis of the southern Mariana Trench. Normal faults continue to grow as the plate moves toward the trench, reaching maximum throws at about 10–35 km from the trench. The calculated nonisostatic topography can be explained by models involving only a vertical load and a bending moment applied at the trench. However, the additional observations of the location of maximum normal fault throw, as well as the prevalence of normal faults dipping toward the southern Mariana Trench can only be explained by models with significant horizontal tensional force, which is calculated to be about 62% of the vertical load for the southern Mariana Trench.

References

Babeyko, A. Y., S. V. Sobolev, R. Trumbull, O. Oncken, and L. Lavier (2002), Numerical models of crustal scale convection and partial melting beneath the Altiplano–Puna plateau, *Earth Planet. Sci. Lett.*, 199, 373–388.

Behn, M. D., and G. Ito (2008), Magmatic and tectonic extension at mid-ocean ridges: 1. Controls on fault characteristics, *Geochem. Geophys. Geosyst.*, 9, Q08O10, doi:10.1029/2008GC001965.

Billen, M. I., and M. Gurnis (2005), Constraints on subducting plate strength within the Kermadec trench, *J. Geophys. Res.*, 110, B05407, doi:10.1029/2004JB003308.

Buck, W. R., and A. N. Poliakov (1998), Abyssal hills formed by stretching oceanic lithosphere, *Nature*, 392, 272–275.

Buck, W. R., L. L. Lavier, and A. N. Poliakov (2005), Modes of faulting at mid-ocean ridges, *Nature*, 434, 719–723.

Choy, G. L., and S. H. Kirby (2004), Apparent stress, fault maturity and seismic hazard for normal-fault earthquakes at subduction zones, *Geophys. J. Int.*, 159, 991–1012.

Contreras-Reyes, E., and A. Osses (2010), Lithospheric flexure modelling seaward of the Chile trench: Implications for oceanic plate weakening in the trench outer rise region, *Geophys. J. Int.*, 182, 97–112.

Cundall, P. A. (1989), Numerical experiments on localization in frictional materials, *Ing. Arch.*, 59, 148–159.

Emry, E. L., D. A. Wiens, and D. Garcia-Castellanos (2014), Faulting within the Pacific Plate at the Mariana Trench: Implications for plate interface coupling and subduction of hydrous minerals, *J. Geophys. Res. Solid Earth*, 119, 3076–3095, doi:10.1002/2013JB010718.

Faccenda, M., L. Burlini, T. V. Gerya, and D. Mainprice (2008), Fault-induced seismic anisotropy by hydration in subducting oceanic plates, *Nature*, 455, 1097–1100.

Faccenda, M., T. V. Gerya, and L. Burlini (2009), Deep slab hydration induced by bending-related variations in tectonic pressure, *Nat. Geosci.*, 2, 790–793.

Forsyth, D., and S. Uyeda (1975), On the relative importance of the driving forces of plate motion, *Geophys. J. R. Astron. Soc.*, *43*, 163–200.

Frohlich, C. (1989), The nature of deep-focus earthquakes, *Annu. Rev. Earth Planet. Sci.*, *17*, 227–254.

Ivandic, M., I. Grevemeyer, A. Berhorst, E. R. Flueh, and K. McIntosh (2008), Impact of bending related faulting on the seismic properties of the incoming oceanic plate offshore of Nicaragua, *J. Geophys. Res.*, *113*, B05410, doi:10.1029/2007JB005291.

Jones, G., T. Hilde, G. Sharman, and D. Agnew (1978), Fault patterns in outer trench walls and their tectonic significance, *J. Phys. Earth*, *26*(suppl), S85–S101.

Kirby, S. H., S. Stein, E. A. Okal, and D. C. Rubie (1996), Metastable mantle phase transformations and deep earthquakes in subducting oceanic lithosphere, *Rev. Geophys.*, *34*, 261–306, doi:10.1029/96RG01050.

Kobayashi, K., M. Nakanishi, K. Tamaki, and Y. Ogawa (1998), Outer slope faulting associated with the western Kuril and Japan trenches, *Geophys. J. Int.*, *134*, 356–372.

Lavier, L. L., W. R. Buck, and A. N. Poliakov (1999), Self-consistent rolling-hinge model for the evolution of large-offset low-angle normal faults, *Geology*, *27*, 1127–1130.

Lavier, L. L., W. R. Buck, and A. N. Poliakov (2000), Factors controlling normal fault offset in an ideal brittle layer, *J. Geophys. Res.*, *105*, 23,431–23,442, doi:10.1029/2000JB900108.

Lay, T., H. Kanamori, C. J. Ammon, A. R. Hutko, K. Furlong, and L. Rivera (2009), The 2006–2007 Kuril Islands great earthquake sequence, *J. Geophys. Res.*, *114*, B11308, doi:10.1029/2008JB006280.

Lay, T., C. J. Ammon, H. Kanamori, L. Rivera, K. D. Koper, and A. R. Hutko (2010), The 2009 Samoa-Tonga great earthquake triggered doublet, *Nature*, *466*, 964–968.

Ludwig, W., et al. (1966), Sediments and structure of the Japan Trench, *J. Geophys. Res.*, *71*, 2121–2137, doi:10.1029/JZ071i008p02121.

Masson, D. G. (1991), Fault patterns at outer trench walls, *Mar. Geophys. Res.*, *13*, 209–225.

McNutt, M. K., and H. W. Menard (1982), Constraints on yield strength in the oceanic lithosphere derived from observations of flexure, *Geophys. J. R. Astron. Soc.*, *71*, 363–394.

Naliboff, J. B., M. I. Billen, T. Gerya, and J. Saunders (2013), Dynamics of outer rise faulting in oceanic-continental subduction systems, *Geochem. Geophys. Geosyst.*, *14*, 2310–2327, doi:10.1002/ggge.20155.

Oakley, A., B. Taylor, and G. Moore (2008), Pacific Plate subduction beneath the central Mariana and Izu-Bonin fore arcs: New insights from an old margin, *Geochem. Geophys. Geosyst.*, *9*, Q06003, doi:10.1029/2007GC001820.

Okal, E. A., D. Reymond, and S. Hongsresawat (2013), Large, pre-digital earthquakes of the Bonin-Mariana subduction zone, 1930–1974, *Tectonophysics*, *586*, 1–14.

Olive, J.-A., M. D. Behn, and B. E. Tucholke (2010), The structure of oceanic core complexes controlled by the depth distribution of magma emplacement, *Nat. Geosci.*, *3*, 491–495.

Poliakov, A. N., and W. R. Buck (1998), Mechanics of stretching elastic–plastic-viscous layers: Applications to slow-spreading mid-ocean ridges, in *Faulting and Magmatism at Mid-Ocean Ridges*, *Geophys. Monogr. Ser.*, vol. 106, edited by W. R. Buck et al., pp. 305–323, AGU, Washington, D. C.

Poliakov, A. N., P. A. Cundall, Y. Y. Podladchikov, and V. A. Lyakhovsky (1993), An explicit inertial method for the simulation of viscoelastic flow: An evaluation of elastic effects on diapiric flow in two- and three-layers models, in *Flow and Creep in the Solar System: Observations, Modeling and Theory*, pp. 175–195, Kluwer Acad., Dordrecht, Netherlands.

Ranero, C. R., J. P. Morgan, K. McIntosh, and C. Reichert (2003), Bending-related faulting and mantle serpentinization at the Middle America Trench, *Nature*, *425*, 367–373.

Ranero, C. R., A. Villaseñor, J. P. Morgan, and W. Weinrebe (2005), Relationship between bend-faulting at trenches and intermediate-depth seismicity, *Geochem. Geophys. Geosyst.*, *6*, Q12002, doi:10.1029/2005GC000997.

Savage, J. C. (1969), The mechanics of deep-focus faulting, *Tectonophysics*, *8*, 115–127.

Supak, S., D. Bohnenstiehl, and W. Buck (2006), Flexing is not stretching: An analogue study of flexure-induced fault populations, *Earth Planet. Sci. Lett.*, *246*, 125–137.

Tucholke, B. E., M. D. Behn, W. R. Buck, and J. Lin (2008), Role of melt supply in oceanic detachment faulting and formation of megamullions, *Geology*, *36*, 455–458.

Turcotte, D., and G. Schubert (2002), *Geodynamics*, 2nd ed., 456 pp., Cambridge Univ. Press, New York.

Van Keken, P. E., B. R. Hacker, E. M. Syracuse, and G. A. Abers (2011), Subduction factory: 4. Depth-dependent flux of H_2O from subducting slabs worldwide, *J. Geophys. Res.*, *116*, B01401, doi:10.1029/2010JB007922.

Wessel, P., and W. H. F. Smith (1998), New improved version of Generic Mapping Tools released, *Eos Trans. AGU*, *79*, 579, doi:10.1029/98EO00426.

Zhang, F., J. Lin, and W. Zhan (2014), Variations in oceanic plate bending along the Mariana Trench, *Earth Planet. Sci. Lett.*, *401*, 206–214.